Full Length Article

# Generating micro/nanostructures on magnesium alloy surface using ultraprecision diamond surface texturing process

Hanheng Du[a], Mengnan Jiang[b], Zuankai Wang[b], Zhiwei Zhu[c,**], Suet To[a,*]

[a] *State Key Laboratory of Ultra-Precision Machining Technology, Department of Industrial and Systems Engineering, The Hong Kong Polytechnic University, Hong Kong, China*
[b] *Department of Mechanical Engineering, City University of Hong Kong, Hong Kong, China*
[c] *School of Mechanical Engineering, Nanjing University of Science and Technology, Nanjing, China*

## Abstract

The lightness and high strength-to-weight ratio of the magnesium alloy have attracted more interest in various applications. However, micro/nanostructure generation on their surfaces remains a challenge due to the flammability and ignition. Motivated by this, this study proposed a machining process, named the ultraprecision diamond surface texturing process, to machine the micro/nanostructures on magnesium alloy surfaces. Experimental results showed the various microstructures and sawtooth-shaped nanostructures were successfully generated on the AZ31B magnesium alloy surfaces, demonstrating the effectiveness of this proposed machining process. Furthermore, sawtooth-shaped nanostructures had the function of inducing the optical effect and generating different colors on workpiece surfaces. The colorful letter and colorful flower image were clearly viewed on magnesium alloy surfaces. The corresponding cutting force, chip morphology, and tool wear were systematically investigated to understand the machining mechanism of micro/nanostructures on magnesium alloy surfaces. The proposed machining process can further improve the performances of the magnesium alloy and extend its functions to other fields, such as optics.

## 1. Introduction

With the ever-increasing demand for lightweight in automotive, electronics, aerospace, biomedical, and other fields, magnesium alloys have received wide attention due to the characteristics of low density, high specific strength, high thermal conductivity, and others [1–4]. Besides, magnesium alloy also possesses many attractive machining properties [5], such as lower machining force and lower machining power required. Lu et al. [6] investigated the effect of cutting parameters on microstructure, machining hardness, and surface roughness, and established a geometrical prediction model of

the roughness in the high-speed cutting of the magnesium alloy. Viswanathan et al. [7] employed the Taguchi method to optimize the turning parameters of the magnesium alloy for minimizing the tool flank wear, surface roughness, and cutting temperature. Turning experiments verified the effectiveness of the Taguchi method on the decrease of these three objectives. Zhang et al. [8] analysed the effect of milling parameters on the chip morphology and the influence of alloy composition on the combustion state during the high-speed milling of the magnesium alloy. Varatharajulu et al. [9] applied the multiple criteria decision-making methods to select the suitable drilling parameters to simultaneously minimize all the responses, such as drilling time and surface roughness.

However, to date, the exploration of micro/nanostructure generation on magnesium alloy surfaces was rarely reported in the literature. There may be several reasons that lead to this situation. Firstly, laser ablation as an advanced machin-

---

* Corresponding authors.
** Corresponding authors.
*E-mail addresses:* zw.zhu@njust.edu.cn (Z. Zhu), sandy.to@polyu.edu.hk (S. To).

ing process with low cost and high flexibility has been widely applied in the microstructure generation of a large number of materials [10,11], but it is not suitable to be employed on the magnesium alloy considering the ignition and flammability of the magnesium alloy. Secondly, although the micro-machining with the natural single-crystal diamond cutting tool is well suited at the micro/nanostructure machining [12,13], the processing time is unacceptable for mass production. Thirdly, the chemical wet etching, as a chemical process, also can fabricate micro/nanostructure on material surfaces [14,15], but the surface quality obtained by this process is difficult to guarantee. Micro/nanostructures can enhance the performance and functionality of the metal surfaces and have been applied in various fields, such as optics [16,17], bioengineering [18,19], tribology [20,21], self-cleaning [22,23], to mention a few. Therefore, how to generate the micro/nanostructures on magnesium alloy surfaces needs to be systematically studied.

Recently, in the field of ultraprecision machining, vibration-assisted machining is drawing attention due to its many advantages, such as the lower cutting force [24], less tool wear [25], burr suppression [26], and improving surface quality [27]. Its working principle is that the periodic vibration trajectory is added to the cutting tool to remove the workpiece material. At the beginning, this process is used to improve the machinability of difficult-to-machine materials, such as Inconel 718 [28], titanium alloy [29], and optical glass [30]. With the development of this process, when the combination of the cutting velocity and vibration trajectory is appropriate, this process also can machine the different micro/nanostructures on the workpiece surface. The vibration generator offers the periodic vibration trajectory into the cutting tool, so it plays a crucial role in this process. According to the working mode of the vibration generator, it is classified as resonant mode and non-resonant mode. The resonant vibration generator works at the natural frequency of the mechanical structure. Shamoto and Moriwaki [31] designed a resonant elliptical vibration generator to generate the elliptical trajectory for fabricating microgroove on the hardened steel. This vibration generator has a working frequency of about 20 kHz. Guo and Ehmann [32] developed a two-degree-of-freedom ultrasonic vibration generator for texturing the microstructures on the metallic surface. However, these resonant mode vibration generators encounter a crucial problem: the working frequency and vibration amplitude are fixed, which obviously limits the flexibility of these devices. To solve this problem, non-resonant vibration generators are fast developing because of the adjustable frequency and vibration amplitude. Kim et al. [33] designed one degree-of-freedom vibration generator installed on the Z-axis of a diamond turning machine. In order to deal with the problem of the small stroke of the piezoelectric actuator, Liu et al. [34] used a voice coil motor as the actuator to design a vibration generator and the sinusoidal surface was machined based on this device. However, these non-resonant vibration generators only offer one-degree-of-freedom vibration trajectory to the cutting tool, which limits the shape diversity of the machined

micro/nanostructures and then influences the functionality of these micro/nanostructures.

To address the above-mentioned issues and generate various micro/nanostructures on magnesium alloy surfaces, an ultraprecision diamond surface texturing process is proposed based on the developed two-degree-of-freedom vibration generator in this study. Then, the finite element model is established to simulate the machining process and evaluate the cutting force in Section 3. The AZ31B, as a typical magnesium alloy, is selected as the workpiece material in this study. Next, to further demonstrate the flexibility of the proposed process, sawtooth-shaped nanostructures are machined to generate different colors on magnesium alloy surfaces and the generation principle of these colors is theoretically illustrated. Finally, after machining experiments, the detailed results on the microstructure topography, cutting force, chip morphology, structural color, and tool wear are discussed in Section 6, followed by main conclusions in Section 7.

## 2. Ultraprecision diamond surface texturing process

Based on vibration-assisted machining, an ultraprecision diamond surface texturing process is proposed in this study to machine micro/nanostructures on the magnesium alloy surface. To realize this process, a hardware platform is established, as shown in Fig. 1(a). In this platform, an ultraprecision lathe that has the nanoscale motion resolution is used to offer the cutting velocity. A natural single-crystal diamond cutting tool with a sharp cutting edge is employed as the cutting tool. A two-degree-of-freedom vibration generator (2DOF-VG) is developed to offer a periodic vibration trajectory. In addition to the above hardware, this hardware platform also includes a drive system of the 2DOF-VG. The drive system is composed of a computer that provides command signals, a multifunction I/O device that converts the command signals into analogue signals, and a piezo amplifier that amplifies the analogue signals.

As a core component of the ultraprecision diamond surface texturing process, the 2DOF-VG plays an important role in machining micro/nanostructures. Its three-dimensional model is shown in Fig. 1(b). It consists of the piezoelectric actuator (PEA), the quasi-ellipse amplification unit (QEAU), and the flexure guidance unit (FGU). When the amplified analogue signal is inputted into the PEA, the PEA can generate the corresponding displacement. The QEAU is utilized to amplify this displacement. The FGU is utilized to transmit the amplified displacement into the cutting tool. Two QEAUs are perpendicularly designed to offer two degree-of-freedoms in the machining plane. Through the sweeping frequency test, it is found that the working frequency of the developed 2DOF-VG can be up to 3000 Hz.

Fig. 1(c) demonstrates the machining principle of the ultraprecision diamond surface texturing process. In this process, the cutting tool will remove the workpiece material and machine micro/nanostructures along the cutting path. Without loss of generality, the cutting path can be mathematically
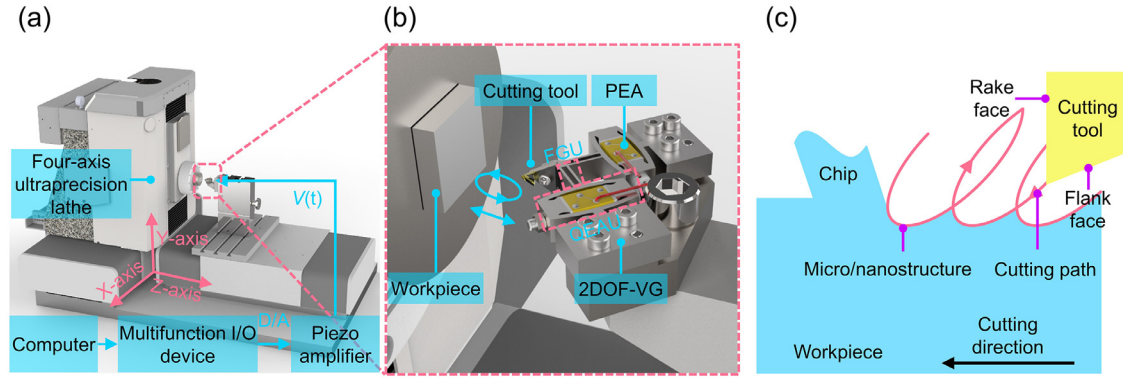
Fig. 1. Ultraprecision diamond surface texturing process. (a) Schematic of hardware platform, (b) close-up views of the two-degree-of-freedom vibration generator, and (c) schematic of micro/nanostructure machining principle.

expressed as:

$$x_{UDST}(t) = d_{UDST}^x(t) + V_{UDST}t \qquad (1)$$

$$z_{UDST}(t) = d_{UDST}^z(t) \qquad (2)$$

where $d_{UDST}^x(t)$ and $d_{UDST}^z(t)$ are the vibration trajectories along the X-axis direction and the Z-axis direction, which are provided by the 2DOF-VG. $V_{UDST}$ is the cutting velocity provided by the ultraprecision lathe. The arbitrary vibration trajectories ($d_{UDST}^x(t)$ and $d_{UDST}^z(t)$) can be realized by the superposition of sinusoidal functions according to the Fourier series. According to Eqs. (1) and (2), the cutting path ($x_{UDST}(t)$, $z_{UDST}(t)$) can be flexibly designed for machining the desired micro/nanostructures on the magnesium alloy surface.

Considering the long time and high frequency working in the machining, the lifetime of the PEA and the material fatigue of the mechanical structure in the 2DOF-VG should be evaluated. For the PEA, the mean time to failure (MTTF), which denotes the expected time to failure, is employed to calculate its average lifetime. MTTF is a function of the applied voltage, the operational temperature, and the relative humidity.

$$\text{MTTF} = f_V \times f_T \times f_H \qquad (3)$$

where $f_V$ is the applied voltage factor, $f_T$ is the operational temperature factor, and $f_H$ is the relative humidity factor. The $f_V$ is calculated by dividing the applied voltage by the maximum drive voltage.

Assuming that the PEA is operated with a voltage of 120 V, at an operational temperature of 26 °C, and in an environment with 75% relative humidity, the three factors ($f_V = 426.8$, $f_T = 138.8$, and $f_H = 2.8$) are obtained from the PEA manufacturers (Thorlabs, Inc.). Then the MTTF can be calculated as 165,871.6 h, which is far larger than the usage time of the PEA.

For the material fatigue of the mechanical structure in the 2DOF-VG, S-N curve is used to analyse the cyclic life of the material. S denotes the stress applied and N denotes the number of cycles before fracture. The maximum stress occurs when the maximal stroke (7 μm) of the PEA is input into



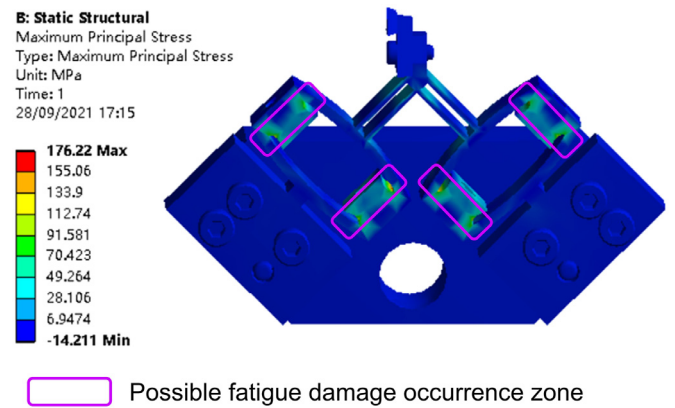Possible fatigue damage occurrence zone

Fig. 2. The maximum stress of the mechanical structure of the two-degree-of-freedom vibration generator.

the mechanical structure. The maximum stress (176.22 Mpa) can be obtained by the finite element simulation software, as shown in Fig. 2. According to the S-N curve of the 304 stainless steel from the reference [35], the number of cycles approaches infinity, demonstrating that there is no fatigue damage occurrence for the mechanical material when the 2DOF-VG works.

## 3. Finite element model

To have a deeper understanding of the ultraprecision diamond surface texturing process, a two-dimensional finite element model is established using the explicit module of the commercial software Abaqus 2021, as shown in Fig. 3. The finite element model includes three parts: the cutting layer of the workpiece, the non-cutting layer of the workpiece, and the cutting tool. To improve the computational efficiency, the meshes in the cutting layer are refined and the meshes in the non-cutting layer are rough. The cutting tool is set as a rigid body and moves along the cutting path. Its rake angle and clearance angle are set as 0° and 15°, respectively, as shown in Fig. 3.

The material flow stress model plays a crucial role in the finite element model [36]. In this study, the Johnson-Cook

Table 1
The properties of the AZ31B magnesium alloy.

| Chemical composition (Weight, %) | | | | Mechanical properties | |
|---|---|---|---|---|---|
| Mg | Balance | Si | 0.16 | Density (Kg/m$^3$) | 1378 |
| Al | 2.96 | Fe | 0.003 | Elastic modulus (GPa) | 44.8 |
| Zn | 0.52 | Cu | 0.006 | Shear modulus (GPa) | 17 |
| Mn | 0.31 | Ni | 0.001 | Poisson's ratio | 0.35 |
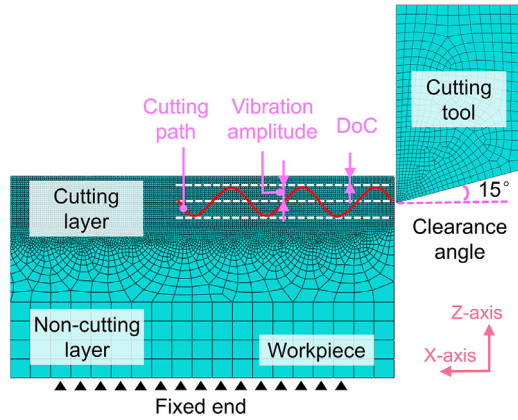


Fig. 3. Finite element model of the ultraprecision diamond surface texturing process.

constitutive model is used to describe the elastoplastic deformation of the material, which considers the strain-strengthening effect, the relationship between flow stress and strain rate, and the relationship between flow stress and temperature [36–38].

$$\sigma_s = \left(A + B\varepsilon_s^n\right)\left[1 + C\ln\left(\frac{\dot{\varepsilon}_s}{\dot{\varepsilon}_0}\right)\right]\left[1 - \left(\frac{T_s - T_0}{T_m - T_0}\right)^m\right] \quad (4)$$

where A, B, C, n, and m are the yield strength constant, hardening modulus constant, strain rate sensitivity coefficient constant, hardening coefficient constant, and thermal softening coefficient, respectively. $\dot{\varepsilon}_s$ is the deformation strain rate. $\dot{\varepsilon}_0$ is the reference shear strain rate that is set as $1.0 \text{ s}^{-1}$ in this study. $T_s$, $T_o$, and $T_m$ are the absolute temperature, room temperature (293 K), and melting temperature (873 K) of the AZ31B magnesium alloy, respectively.

In addition, the Johnson-Cook damage model is employed to realize the workpiece material separation from the cutting layer [39,40].

$$\varepsilon_f = \left[D_1 + D_2\exp\left(D_3\frac{\sigma_m}{\bar{\sigma}}\right)\right]\left[1 + D_4\ln\left(\frac{\dot{\varepsilon}_s}{\dot{\varepsilon}_0}\right)\right]$$
$$\times \left[1 + D_5\left(\frac{T_s - T_0}{T_m - T_0}\right)\right] \quad (5)$$

where the $D_1$–$D_5$ are the Johnson-Cook damage constants. $\sigma_m$ and $\bar{\sigma}$ are the average normal stress and von Mises equivalent stress, respectively. When the equivalent plastic strain is larger than the damage strain $\varepsilon_f$, the material begins to fracture. The material properties and the parameters of the Johnson-Cook constitutive model and the Johnson-Cook damage model for AZ31B magnesium alloy are listed in Tables 1 and 2.

The surface-to-surface contact condition is utilized and the two region zones, i.e., the sticking zone and the sliding zone, are applied to describe the contact between the cutting tool and the chips. The friction at the interface of the cutting tool and chips is controlled by the Coulomb law that is expressed as follows [41]:

$$\tau_f = \begin{cases} \tau_s, & \mu\sigma_n \geq \tau_s \text{ (sticking zone)} \\ \mu\sigma_n, & \mu\sigma_n < \tau_s \text{ (sliding zone)} \end{cases} \quad (6)$$

where $\tau_f$ is the frictional stress. $\tau_s$ is the ultimate shear flow stress. $\mu$ is the friction coefficient between the cutting tool and workpiece, which is set as 0.2 in this study. $\sigma_n$ is the normal stress on the contact surface.

The cutting path of the cutting tool is given in Eqs. (1) and (2). In the software Abaqus, the periodic amplitude function is utilized to load the vibration trajectory of the 2DOF-VG [42].

$$a = \begin{cases} A_0 + \sum_{n=1}^{N}\left[A_n\cos n\omega(t - t_0) + B_n\sin n\omega(t - t_0)\right], & t \geq t_0 \\ A_0, & t < t_0 \end{cases} \quad (7)$$

where $A_0$ is the initial amplitude, $\omega$ is the circular frequency, $t_0$ is the starting time. $A_n$ and $B_n$ are the coefficients of the cosine and sine functions. N is the number of Fourier series terms. The "Dynamic, temp-disp, explicit" method is utilized to solve the finite element model.

## 4. Structural color generation principle

Nanostructures with specific facet spacing have an optical effect and can induce different color generation on the workpiece surface. The color induced by the nanostructure is named structural color. In order to demonstrate the flexibility of the ultraprecision diamond surface texturing process and machine the optically functional nanostructures, the structural color generation on the magnesium alloy surface is studied, which can extend the application range of the magnesium alloy to optics.

Fig. 4 demonstrates how to generate structural color on the workpiece surface. Firstly, the size of the original image needs to be compressed to suit the workpiece size, as shown in Fig. 4(a). In general, the small the single-pixel size, the high resolution the structural color. However, the machining time dramatically increases with the increase of the resolution. In this study, the single-pixel size is set as 70 μm to comprehensively balance the machining time and the resolution. Then, the RGB values of the compressed image are sorted

Table 2
Johnson-Cook constants of the AZ31B magnesium alloy [43].

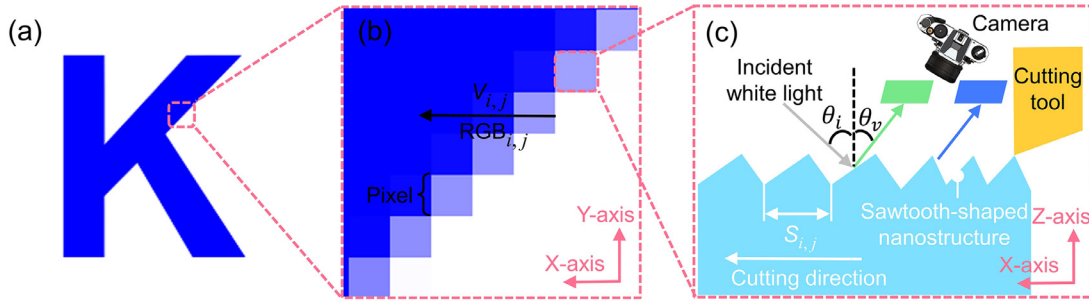| A (MPa) | B (MPa) | $n$ | $m$ | $C$ | $D_1$ | $D_2$ | $D_3$ | $D_4$ | $D_5$ |
|---------|---------|------|-----|-------|-------|--------|-------|-------|-------|
| 153 | 291.8 | 0.1026 | 1.5 | 0.013 | 0.5 | 0.2895 | 3.719 | 0.013 | 1.5 |



Fig. 4. Generation principle of the structural color.

into 16 different levels. The different level corresponds to the different facet spacing ($S_{i,j}$) of nanostructures. The facet spacing can be simultaneously controlled by the cutting velocity ($V_{i,j}$) that the ultraprecision lathe provides and the vibration frequency ($f$) that the 2DOF-VG provides. So, there are two methods, i.e., adjusting the cutting velocity or adjusting the vibration frequency, to control the facet spacing according to Eq. (8). Since adjusting the cutting velocity is easier to realize through the velocity commands of the ultraprecision lathe, the cutting velocity is chosen to control the facet spacing according to the RGB value of each pixel in this study and the vibration frequency keeps constant.

$$S_{i,j} = V_{i,j}/f \tag{8}$$

After $i$th line machining, the cutting tool feeds a single-pixel size along the Y-axis of the ultraprecision lathe, as shown in Fig. 4(b). The cycle begins until finish the whole structural color machining on the workpiece surface.

In essence, the structural color can be viewed due to the physical interaction between the visible light and the sawtooth-shaped nanostructure, as shown in Fig. 4(c). It can be described by the grating equation [44,45]:

$$\sin\theta_i + \sin\theta_v = m\lambda_{i,j}/S_{i,j} (m = 0, \pm 1, \pm 2, \pm 3, \ldots) \tag{9}$$

where $\theta_i$ and $\theta_v$ are the incident angle and viewing angle. $m$ is the reflection order. $\lambda_{i,j}$ is the wavelength of the reflection light.

The white light with different wavelengths is applied as the incident light and the sawtooth-shaped nanostructure plays a role as the reflection grating. Assuming that $\theta_i = 0$ and $m = 1$, the wavelength $\lambda_{i,j}$ of a certain color can be derived as:

$$\lambda_{i,j} = S_{i,j}\sin\theta_v \tag{10}$$

A certain color can be observed when the facet spacing is $S_{i,j}$. Therefore, the different colors can be flexibly generated by controlling the facet spacing of sawtooth-shaped nanostructures.

## 5. Experimental procedures

The experiments were performed on the hardware platform, as shown in Fig. 5. The AZ31B magnesium alloy cube (Keple Technology Co., Ltd., China) with dimensions of $15 \times 15 \times 5$ mm$^3$ was glued into a fixture, which was stationed on the spindle of the four-axis ultraprecision lathe (350FG, Moore Nanotechnology). For obtaining a proper planer surface with high surface quality, the workpiece was pre-machined with a spindle speed of 1400 rpm using the ultraprecision turning process. The depth-of-cutting and feed rate were set as 2 µm and 2 mm/min for the pre-machining. The nose radius of the used single-crystal diamond cutting tool (Apex Diamond Products Ltd.) is 0.509 mm. In the micro/nanostructure machining, the developed 2DOF-VG was mounted on the dynamometer via a screw. The computer provided command signals, which were converted into analog signals by the multifunction I/O device (USB-6341, National Instruments Corp.). Then they were magnified by the piezo amplifiers (E617.001, Physik Instrumente GmbH & Co.KG). The magnified analog signals were inputted into the PEA (PK4FA2H3P2, Thorlabs Inc.) to drive the 2DOF-VG. In the ultraprecision diamond surface texturing process, two single-crystal diamond cutting tools with different nose radii were applied. The cutting tool with a nose radius of 0.515 mm (N0.50mLEi, Contour Fine Tooling Inc.) was used to machine microstructures on the magnesium alloy surface. The cutting tool with a nose radius of 0.223 mm (N0.20mLEi, Contour Fine Tooling Inc.) was used to machine the sawtooth-shaped nanostructures to generate the structural colors. The detailed machining parameters are listed in Table 3. When finishing one cutting motion, the cutting tool would return to the origin point in the X-axis and feed a pitch (named as cross-feed) along Y-axis and the cycle starts again.

The cutting forces were measured through the Kistler force measurement system, which consists of this dynamometer (9256C1, Kistler Instrument Corp.), a charge amplifier (5080, Kistler Multichannel Charge amplifier), and PC software
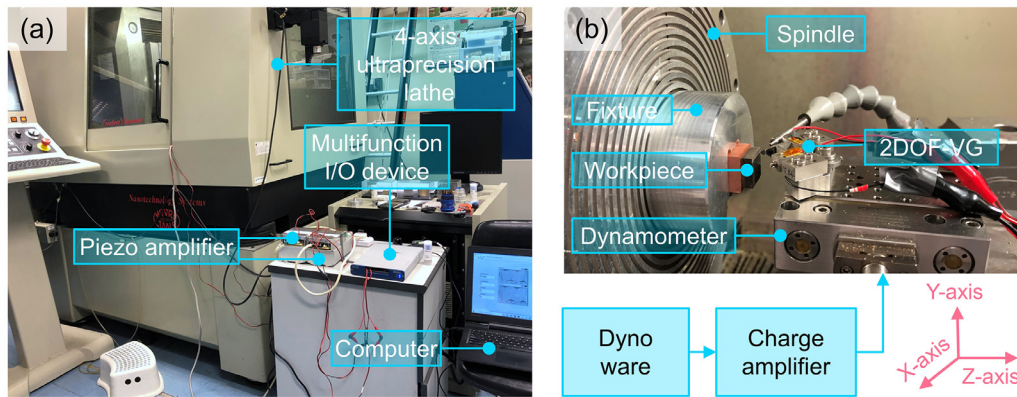
Fig. 5. The experiment setup of the micro/nanostructure machining. (a) Full-view and (b) close-up view.

Table 3
The machining parameters.

|  | Case1 | Case2 | Case3 | Structural color machining |
|---|---|---|---|---|
| Cutting speed (mm/min) | 500 | 500 | 500 | Varying |
| Depth-of-cutting (mm) | 0.004 | 0.004 | 0.004 | 0.003 |
| Cross-feed (mm) | 0.160 | 0.160 | 0.160 | 0.07 |
| Voltage amplitude (V) | 40 | 40 | 40 | 30 |
| Vibration frequency (Hz) | 300 | 300 | 300 | 1000 |
| Phase difference | 0° | 90° | 180° | 0° |

(Dyno ware), as shown in Fig. 5(b). The sampling rate of capturing cutting force data was set as 50 kHz for sufficiently collecting the cutting forces. As the force sensor may have electrical drift which means the zero point of the output signal may move to a positive or negative value during experiments, the software Dyno ware was used to compensate for this electrical drift. After the experiments, the workpieces were cleaned in the ultrasonic cleaner using alcohol for 10 min. A scanning electron microscope (SEM) (Hitachi Electron Microscope TM3000) was utilized to observe the chips and the tool wear. The Renishaw micro-Raman spectroscopy system was employed to analyse the tool wear mechanism. The Raman scattering spectrum range was set at from 600 to 2300 $cm^{-1}$ with a spectral resolution of 0.3 $cm^{-1}$.

## 6. Results and discussion

### 6.1. Microstructure topography characterization

Fig. 6(a–c) show the optical micrographs of various microstructures on the magnesium alloy surface. The insets in the top right of Fig. 6(a–c) show the magnification images of microstructures, which give the clear view of their topography. For Case 1 and Case 2, the main features (shape and layout) look similar, but the edges of microstructures display obvious differences. Case 1 shows the sharp and linear-shaped edges while Case 2 shows the smooth and curved-shaped edges, as marked using the red line. The shape of microstructures in Case 3 looks like the bamboo, which is totally different from both Case 1 and Case 2. Besides, the cross-sectional profiles passing through the center of mi-

crostructure were extracted and plotted in Fig. 6(d–f). It can be found that these microstructures have different heigh besides the different profile shapes. Different vibration trajectories caused by the phase difference lead to these results. The vibration trajectory in Case 1 is the straight-line motion along the Z-axis direction (depth-of-cutting direction), while the two-dimensional elliptical trajectory in Case 2 is generated along the X-axis direction (cutting direction) and Z-axis direction. The elliptical trajectory creates smooth and curved edges. The vibration trajectory in Case 3 is also a straight-line motion but its direction is along the X-axis direction, so the bamboo-shaped microstructures distributing in the X-axis direction can be generated. Further, the increasing phase difference also causes the decrease in vibration amplitude of 2DOF-VG along the depth-of-cutting direction, which brings about a decrease in the height of microstructures.

The theoretical value of the facet spacing can be calculated (27.8 μm) according to Eq. (8). The corresponding measured results are 27.6 μm in Case1, 28.1 μm in Case2, and 27.9 μm in Case3, respectively. Therefore, the relative errors with respect to the theoretical value are 0.72, 1.08, and 0.36%, which indicates that the proposed machining process has high machining accuracy.

### 6.2. Cutting force analysis

Cutting force is a significant indication to monitor the machining process. Fig. 7 shows the measured and simulated cutting forces of the above three cases. $F_x$ and $F_z$ represent the cutting forces along the X-axis direction and Z-axis direction, respectively. The simulated cutting forces are obtained
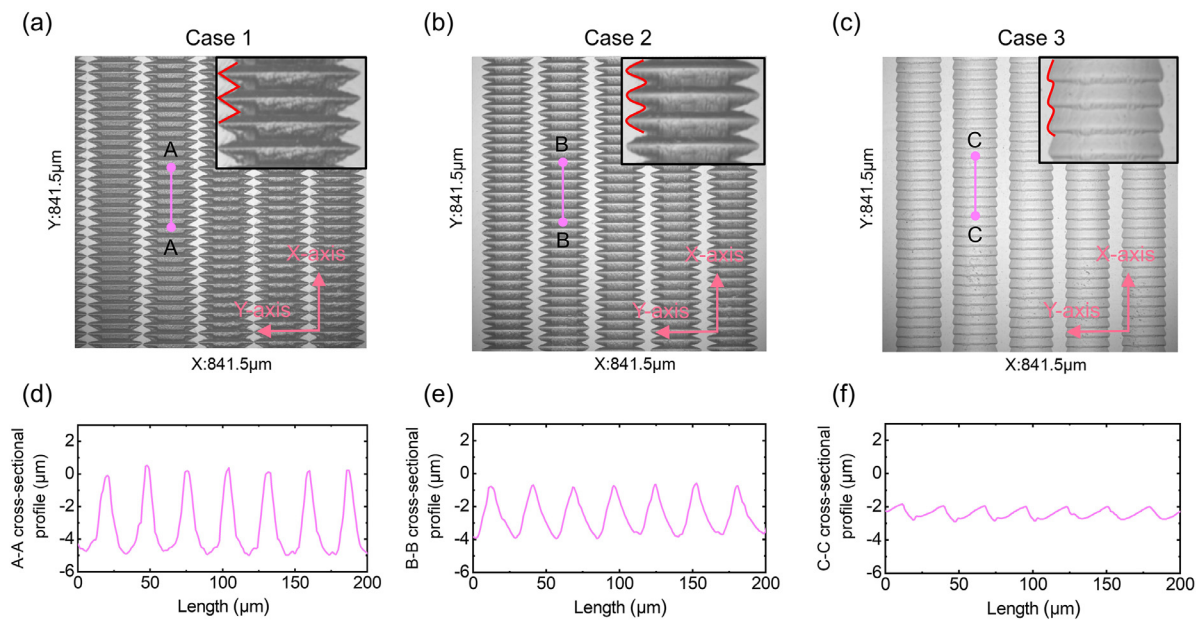
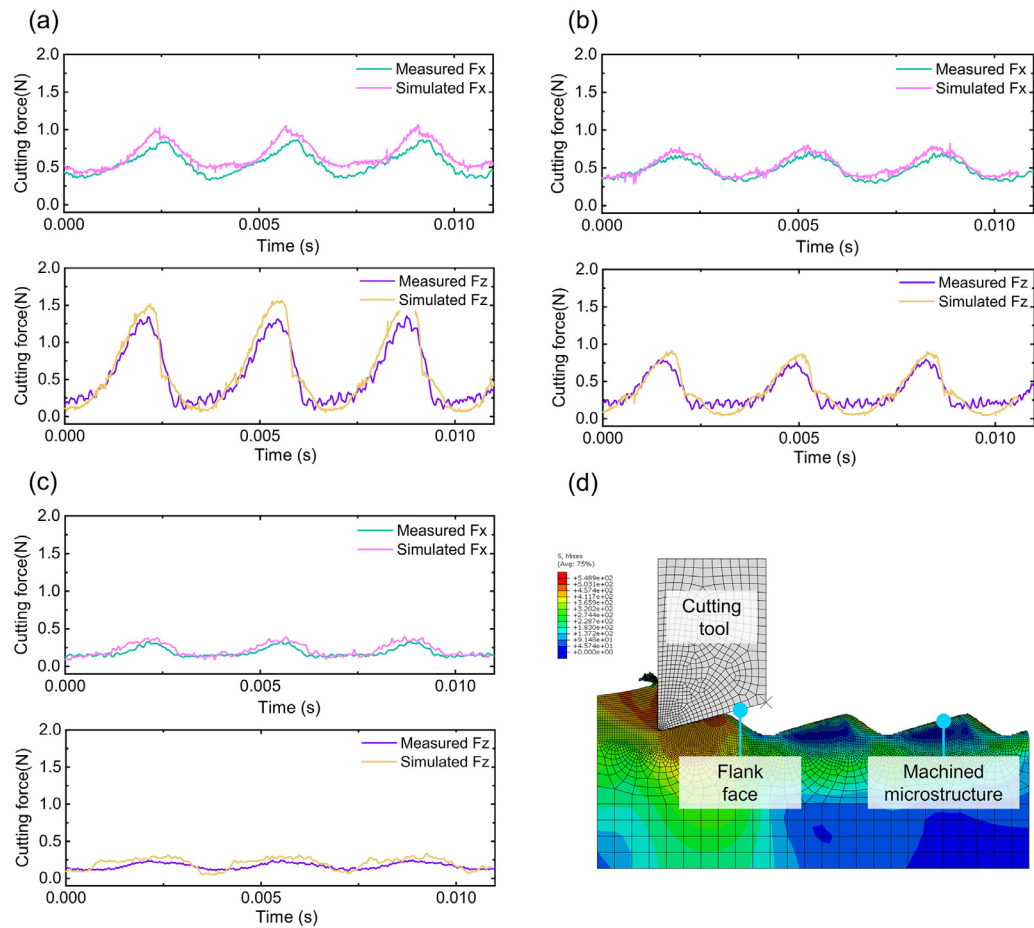Fig. 6. Optical micrographs and cross-sectional profiles of microstructures.



Fig. 7. The measured and simulated cutting forces. (a) Case 1, (b) Case 2, (c) Case 3, and (d) snapshot of the simulated machining process in Case1.

by inputting the identical machining parameters into the finite element model. It is observed that the cutting forces periodically increase and decrease, and the cycle time (3.33 ms) of cutting forces is in accordance with the vibration period (3.33 ms) of the 2DOF-VG. The removal of material begins as soon the cutting tool touches the magnesium alloy surface. The cutting forces increase when the cutting tool advances into the workpiece as more amount of workpiece materials are removed. The cutting forces decrease with the reduction of the material removal volume. When the phase difference changes (0° in Case1, 90° in Case2, and 180° in Case3), the effects on the cutting force are also obvious in the value size and shape trend, as shown in Fig. 7(a–c). Both $F_x$ and $F_z$ reduce with the increase of the phase difference from 0° to 180°. It is because the increase of the phase difference leads to the decrease of the depth-of-cutting, which causes the reduction of the material removal volume. Fig. 7(d) shows the simulated machining process of the ultraprecision diamond surface texturing in Case1.

Besides, the simulated cutting forces using the finite element model show good agreement with the measured cutting force. The average peak-to-valley values of the simulated and measured $F_x$ in Case 1 are 0.56 N and 0.52 N, and that of the simulated and measured $F_z$ in Case 1 are 1.53 N and 1.34 N. The model errors of $F_x$ and $F_z$ in Case 1 can be quantitatively calculated to be 7.69% and 14.18%, respectively. Similarly, the model errors of $F_x$ and $F_z$ in Case 2 and Case 3 are 11.33%, 10.55%, 18.62%, and 18.27%, respectively, which demonstrates the effectiveness of the finite element model on the cutting force simulation during the microstructure machining.

### 6.3. Chip morphology investigation

Chip investigation is another indication to reflect the machining process during the microstructure machining. The chips in the ultraprecision turning process and the ultraprecision diamond surface texturing process are collected. Their morphologies are shown in Fig. 8. As can be seen from the SEM images, fracture features at the side of chips are formed in both machining processes as evidenced by the plastic shearing. The ultraprecision turning process produces very long and continuous chips, and their shape looks like the folded long ribbon. The ultraprecision diamond surface texturing process produces shorter and discontinuous chips. Since the depth-of-cutting dynamically changes with the vibration trajectory in the ultraprecision diamond surface texturing process, the thickness of chips changes with time. The uneven thickness leads to the uneven stiffness of chips. Chips will break at the place with small stiffness. The magnification image in Fig. 8(b) shows the lamellar structure along the chip flow direction and each lamellar structure contains many segments, which demonstrates that the ultraprecision diamond surface texturing process is different from the ultraprecision turning process. Ultraprecision diamond surface texturing process possesses the time-varying depth-of-cutting. Furthermore, there are no burn marks of chips for all experi-

ments, which indicates that the ultraprecision diamond surface texturing process is safe, and no fire hazard exists.

### 6.4. Structural color observation

Before the sawtooth-shaped nanostructure machining, an optical mirror surface with the surface roughness of 0.003 μm was firstly obtained using the ultraprecision turning process to guarantee surface finish, as shown in Fig. 9(a). For obtaining the cutting velocity that each pixel corresponds, as described in Section 4, the viewing angle $\theta_v$ was assumed to be 45°, and the longest visible wavelength (deep red) and shortest visible wavelength (deep violet) were set as 700 nm and 400 nm, respectively. The 16 levels of the RGB values are evenly distributed between 400 and 700 nm. According to Eqs. (8) and (10), the cutting velocity $V_{i,j}$ with respect to the RGB value of each pixel can be calculated. Then the position and velocity commands can be generated accordingly. Besides, the machined regions display vivid colors while the non-machined regions remain the original color of the magnesium alloy, which can be controlled by adjusting the depth-of-cut. Fig. 9(b) shows the letters "SKL", "HKPU", and "Mg alloy" in different colors, which are captured by a digital camera. Fig. 9(c) shows the colorful flower on magnesium alloy surface without using any coating material and pigment. The machining times for these two samples are 41 min and 39 min, respectively, which demonstrates that the proposed machining process is a very highly efficient machining method.

To investigate the three-dimensional morphologies of nanostructures that induce the different color generation, an atomic force microscope (AFM) (Park XE-70, Park Systems, Inc.) was employed. Fig. 10 shows the three-dimensional morphology of nanostructures on the letter "S" and "M" in Fig. 9. It can be clearly found that these nanostructures have periodic sawtooth-like profiles. The average facet spacings of the nanostructures in the letter "S" and "M" are 625 nm and 737 nm, which agree well with the theoretical results (612 and 744 nm). These sawtooth-shaped nanostructures further demonstrate the proposed ultraprecision diamond surface texturing process has the capability of flexibly generating micro/nanostructures on magnesium alloy surfaces.

### 6.5. Tool wear mechanism exploration

Fig. 11(a) and (b) show SEM images of the new cutting tool from the two viewing angles. A very sharp cutting edge between the rake face and flank face can be observed. After the microstructure machining experiments, the micro-chipping and flank wear are clearly found, as shown in Fig. 11(c) and (d). The worst wear occurs on the apex of the cutting tool and then spreads along the cutting edge. The wear volume of the rake face is larger than that of the flank face since the rake face plays the main role in removing the material during the machining, which is described in Fig. 1(c).

To further explore the tool wear mechanism associated with micro/nanostructure machining of the magnesium al-
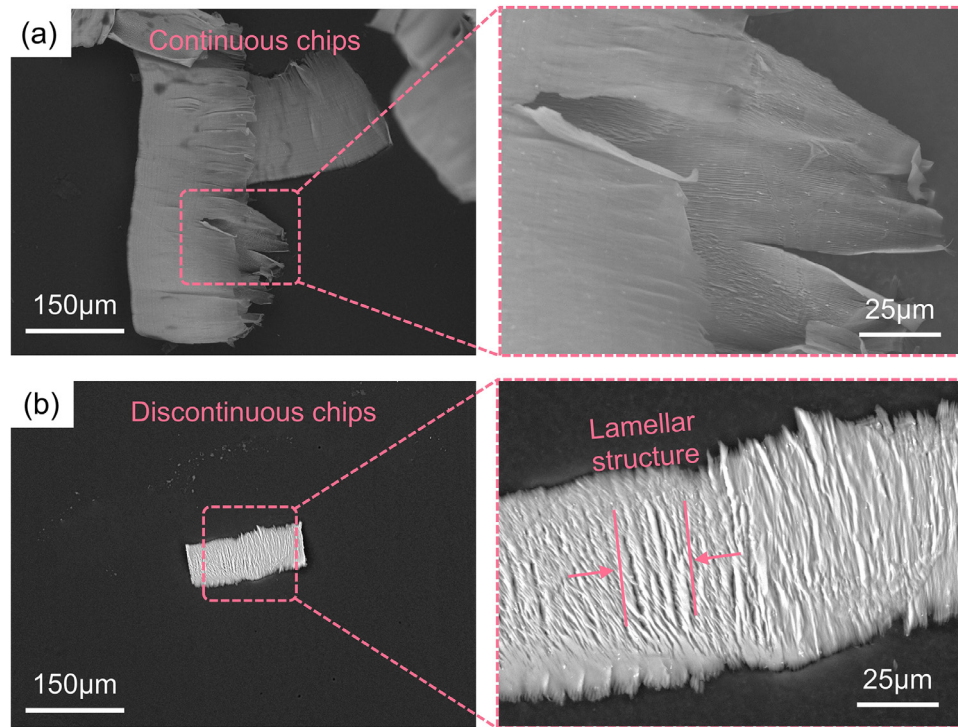
Fig. 8. SEM images of the chip morphology. (a) The ultraprecision turning process and (b) the ultraprecision diamond surface texturing process.
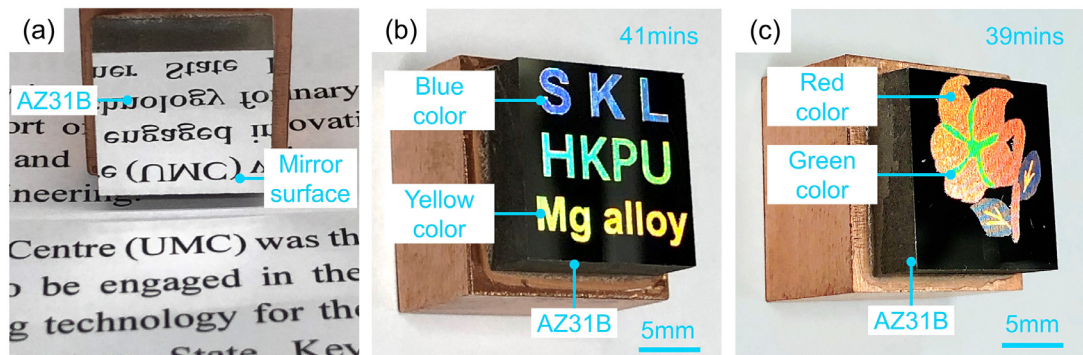


Fig. 9. Photographs of (a) mirror surface, (b) colorful letters "SKL", "HKPU", and "Mg alloy", and (c) colorful flower.

loy, Raman spectroscopy was employed to find possible microstructural changes of the diamond [46]. The Raman spectrum on the rake face of the new cutting tool exhibits a very sharp and single peak at 1332 cm$^{-1}$, as shown in Fig. 12(a). When the laser of the Renishaw micro spectrometer was focused on the "A" point of the tool wear zone in Fig. 11(c), it is seen from Fig. 12(b) that the single peak becomes two peaks, called D-band and G-band. They are located at around 1354 cm$^{-1}$ and 1583 cm$^{-1}$, respectively. The D-band and G-band provide direct evidence for the diamond-graphite transformation of the cutting tool. Therefore, it is concluded that the tool wear in the micro/nanostructure machining of the AZ31B magnesium alloy is related to the diamond graphitization. There are two factors to cause diamond graphitization: high temperature and high pressure. The surface temperature of the workpiece is almost kept at around 21 °C, which is measured by an infrared thermometer. The cutting tool-workpiece interface area is extremely small in the micro/nanostructure machining of the magnesium alloy. So, the high pressure may lead to the graphitization of the partial diamond crystal [47,48].

## 7. Conclusions

In this work, the ultraprecision diamond surface texturing process was proposed to machine the various micro/nanostructures on magnesium alloy surfaces. The systematic study on micro/nanostructure generation, cutting force analysis, chip morphology, and tool wear was carried out. The main conclusions have been drawn:

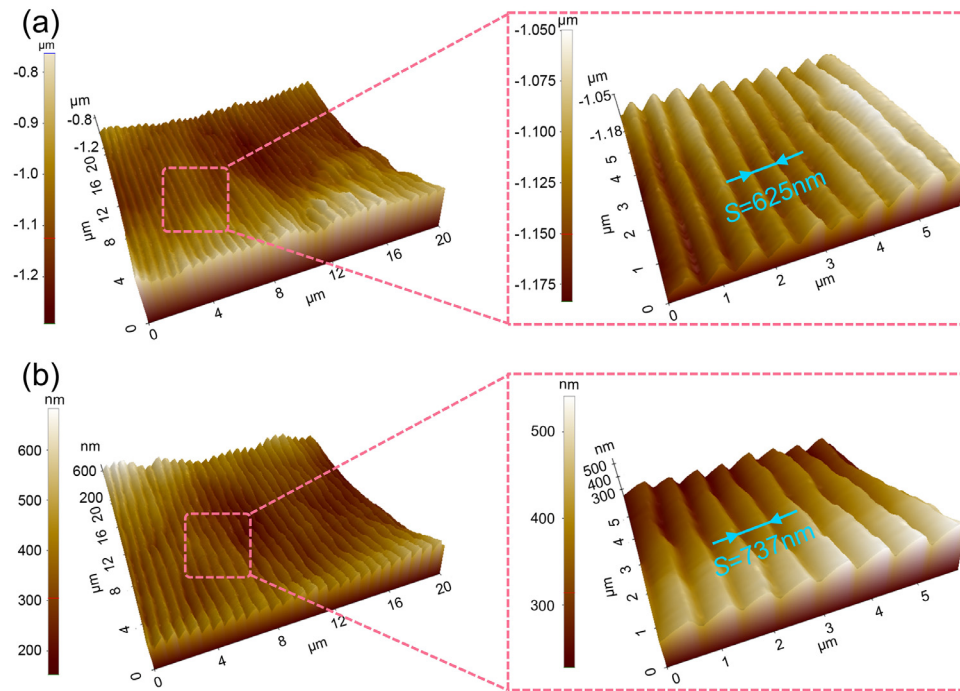(1) A two-degree-of-freedom vibration generator with a working frequency of 3000 Hz was developed to offer

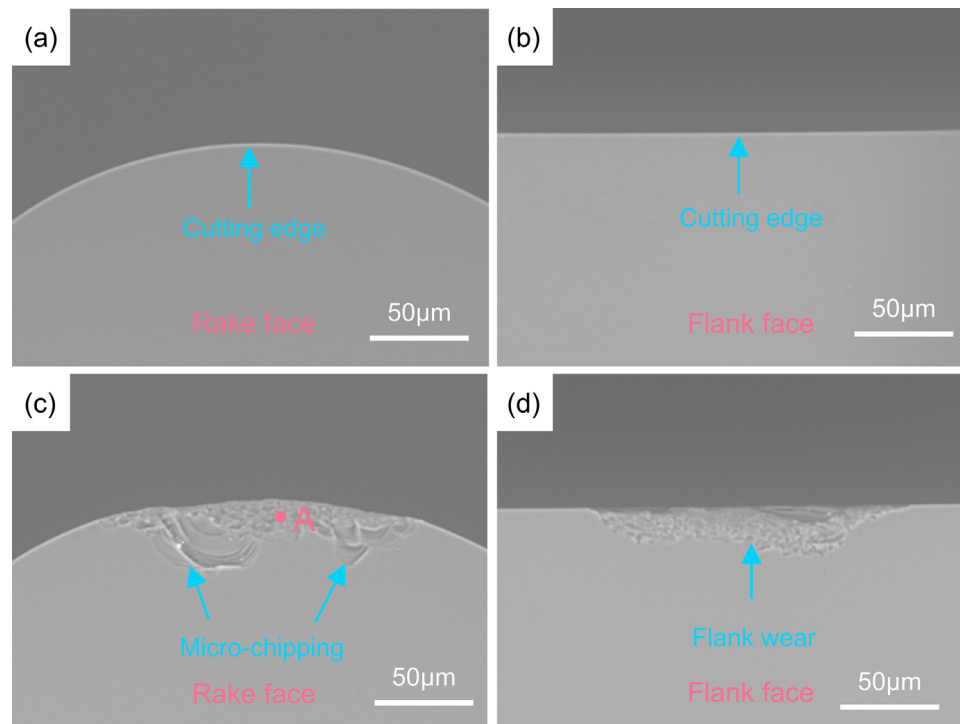Fig. 10. AFM images of nanostructures of (a) letter "S" in Fig. 9 and (b) letter "M" in Fig. 9.



Fig. 11. SEM images of the single-crystal diamond cutting tool. (a) Rake face of the new cutting tool, (b) flank face of the new cutting tool, (c) rake face of the worn cutting tool, and (d) flank face of the worn cutting tool.

the periodic vibration trajectory in the ultraprecision diamond surface texturing process. As a reliability index, the mean time to failure of this device was analysed (more than 160,000 h), which was far larger than its normal use time.

(2) A finite element model was established to simulate the micro/nanostructure machining and the corresponding cutting forces. The experimental results showed the simulated cutting forces were in good agreement with the measured results. The maximal value of cutting forces
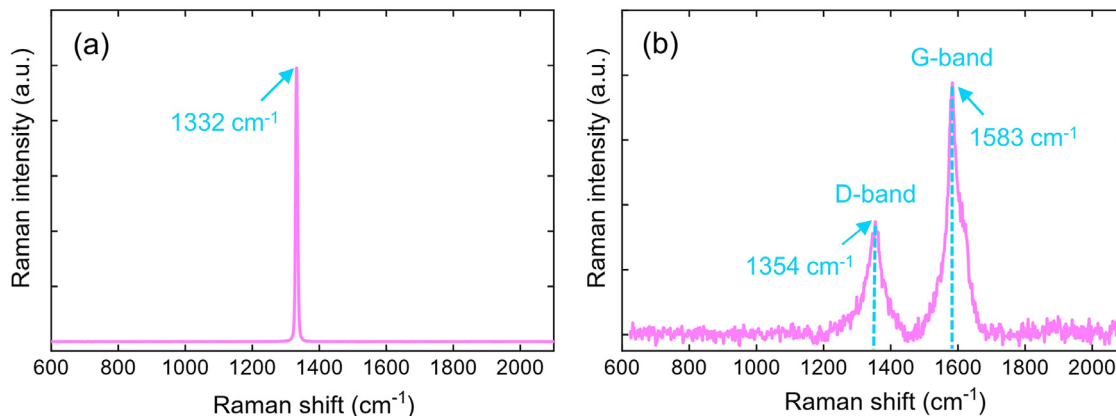
Fig. 12. Raman spectrum of (a) the new single-crystal diamond cutting tool and (b) the worn single-crystal diamond cutting tool.

in all cases was less than 2 N, demonstrating that the magnesium alloy possesses better machinability.

(3) Different shape microstructures (dimple-shaped microstructures and bamboo-shaped microstructures) were successfully machined on magnesium alloy surfaces, showing the effectiveness of the proposed ultraprecision diamond surface texturing process.

(4) Sawtooth-shaped nanostructures were also machined, which induced the different color generation by manipulating the facet spacing of nanostructures. The colorful letters "SKL", "HKPU", and "Mg alloy" as well as colorful flower were observed on workpiece surfaces, which could expand the application range of the magnesium alloy to the field of optics. And the corresponding generation principle of these colors was also in-detail illustrated.

Besides, the graphitization of the single-crystal diamond cutting tool in the machining of micro/nanostructures was found, which may be the reason for the tool wear. This study provides an effective and flexible machining method for generating micro/nanostructures on magnesium alloy surfaces, which are potentially applied to optics, information display, functional decoration, biomedicines, etc.

## Declaration of competing interest

The authors declare that they have no known competing financial interests or personal relationships that could have appeared to influence the work reported in this paper.

## CRediT authorship contribution statement

**Hanheng Du:** Conceptualization, Methodology, Software, Validation, Formal analysis, Investigation, Data curation, Writing – original draft, Writing – review & editing. **Mengnan Jiang:** Writing – review & editing. **Zuankai Wang:** Supervision. **Zhiwei Zhu:** Supervision, Funding acquisition. **Suet To:** Supervision, Funding acquisition.

## References

[1] T.T.T. Trang, J.H. Zhang, J.H. Kim, A. Zargaran, J.H. Hwang, B.C. Suh, N.J. Kim, Nat. Commun. 9 (2018), doi:10.1038/s41467-018-04981-4.

[2] Y. Wang, F. Li, N. Bian, H.Q. Du, P. Da Huo, J. Magnes. Alloy. (2021), doi:10.1016/J.JMA.2021.08.035.

[3] W. Xu, N. Birbilis, G. Sha, Y. Wang, J.E. Daniels, Y. Xiao, M. Ferry, Nat. Mater. 14 (2015) 1229–1235, doi:10.1038/nmat4435.

[4] S.C. Cagan, C.I. Pruncu, B.B. Buldum, J. Magnes. Alloy. 8 (2020) 1061–1070, doi:10.1016/J.JMA.2020.06.008.

[5] S. Tekumalla, N. Gupta, M. Gupta, J. Alloy. Compd. 831 (2020), doi:10.1016/j.jallcom.2020.154840.

[6] L. Lu, S. Hu, L. Liu, Z. Yin, J. Magnes. Alloy. 4 (2016) 128–134, doi:10.1016/J.JMA.2016.04.004.

[7] R. Viswanathan, S. Ramesh, V. Subburam, Measurement 120 (2018) 107–113, doi:10.1016/J.MEASUREMENT.2018.02.018.

[8] H. Zhang, P. Zhao, Y. Ge, H. Tang, Y. Shi, Int. J. Adv. Manuf. Technol. 95 (2018) 3943–3952, doi:10.1007/s00170-017-1511-7.

[9] M. Varatharajulu, M. Duraiselvam, M.B. Kumar, G. Jayaprakash, N. Baskar, J. Magnes. Alloy. (2021), doi:10.1016/J.JMA.2021.05.006.

[10] Z. Zhang, Q. Zhang, Q. Wang, Y. Fu, J. Xu, Opt. Laser Technol. 138 (2021) 106839, doi:10.1016/J.OPTLASTEC.2020.106839.

[11] X. Chen, X. Li, P. Zuo, M. Liang, X. Li, C. Xu, Y. Yuan, S. Wang, ACS Appl. Mater. Interfaces 13 (2021) 13781–13791, doi:10.1021/acsami.0c22080.

[12] A. Meier, Precis. Eng. 42 (2015) 253–260, doi:10.1016/J.PRECISIONENG.2015.05.007.

[13] Y. Wang, Q. Zhao, Y. Shang, P. Lv, B. Guo, L. Zhao, J. Mater. Process. Technol. 211 (2011) 2152–2159, doi:10.1016/J.JMATPROTEC.2011.07.018.

[14] H. Zhang, N.A. Amro, S. Disawal, R. Elghanian, R. Shile, J. Fragala, Appl. Surf. Sci. 253 (2006) 1960–1963, doi:10.1016/J.APSUSC.2006.03.045.

[15] A. Ghafarinazari, M. Mozafari, J. Alloy. Compd. 616 (2014) 442–448, doi:10.1016/J.JALLCOM.2014.07.044.

[16] Z. Zhu, X. Zhou, Z. Liu, R. Wang, L. Zhu, Precis. Eng. 38 (2014) 809–820, doi:10.1016/j.precisioneng.2014.04.009.

[17] Z. Zhu, S. To, Opt. Express 23 (2015) 20234, doi:10.1364/oe.23.020234.

[18] A.H.A. Lutey, L. Gemini, L. Romoli, G. Lazzini, F. Fuso, M. Faucon, R. Kling, Sci. Rep. 8 (2018) 1–10, doi:10.1038/s41598-018-28454-2.

[19] A. Malshe, K. Rajurkar, A. Samant, H.N. Hansen, S. Bapat, W. Jiang, CIRP Ann. Manuf. Technol. 62 (2013) 607–628, doi:10.1016/j.cirp.2013.05.008.

[20] R. Zhou, J. Cao, Q.J. Wang, F. Meng, K. Zimowski, Z.C. Xia, J. Mater. Process. Technol. 211 (2011) 1643–1649, doi:10.1016/J.JMATPROTEC.2011.05.004.

[21] A. Ramesh, W. Akram, S.P. Mishra, A.H. Cannon, A.A. Polycarpou, W.P. King, Tribol. Int. 57 (2013) 170–176, doi:10.1016/j.triboint.2012.07.020.

[22] H. Chen, P. Zhang, L. Zhang, H. Liu, Y. Jiang, D. Zhang, Z. Han, L. Jiang, Nature 532 (2016) 85–89, doi:10.1038/nature17189.

[23] S. Liu, X. Zhang, S. Seeger, ACS Appl. Mater. Interfaces 11 (2019) 47, doi:10.1021/acsami.9b15318.

[24] M. Zhou, Y.T. Eow, B.K.A. Ngoi, E.N. Lim, Mater. Manuf. Process. 18 (2003) 825–834, doi:10.1081/AMP-120024978.

[25] M. Zhou, B.K.A. Ngoi, M.N. Yusoff, X.J. Wang, J. Mater. Process. Technol. 174 (2006) 29–33, doi:10.1016/J.JMATPROTEC.2005.02.248.

[26] C. Ma, E. Shamoto, T. Moriwaki, Y. Zhang, L. Wang, Int. J. Mach. Tools Manuf. 45 (2005) 1295–1300, doi:10.1016/J.IJMACHTOOLS.2005.01.011.

[27] Z. Yang, L. Zhu, G. Zhang, C. Ni, B. Lin, Int. J. Mach. Tools Manuf. 156 (2020) 103594, doi:10.1016/J.IJMACHTOOLS.2020.103594.

[28] C. Nath, M. Rahman, Int. J. Mach. Tools Manuf. 48 (2008) 965–974, doi:10.1016/J.IJMACHTOOLS.2008.01.013.

[29] R. Muhammad, M.S. Hussain, A. Maurotto, C. Siemers, A. Roy, V.V. Silberschmidt, J. Mater. Process. Technol. 214 (2014) 906–915, doi:10.1016/J.JMATPROTEC.2013.12.002.

[30] J. Wang, P. Feng, J. Zhang, J. Manuf. Process. 32 (2018) 213–221, doi:10.1016/J.JMAPRO.2018.02.001.

[31] E. Shamoto, T. Moriwaki, CIRP Ann. 48 (1999) 441–444, doi:10.1016/S0007-8506(07)63222-3.

[32] P. Guo, K.F. Ehmann, Precis. Eng. 37 (2013) 364–371, doi:10.1016/j.precisioneng.2012.10.005.

[33] H.S. Kim, K.I. Lee, K.M. Lee, Y.B. Bang, Int. J. Mach. Tools Manuf. 49 (2009) 991–997, doi:10.1016/j.ijmachtools.2009.06.011.

[34] Q. Liu, X. Zhou, Z. Liu, C. Lin, L. Ma, Opt. Eng. 53 (2014) 092005, doi:10.1117/1.oe.53.9.092005.

[35] Y. Oshida, A. Deguchi, Fatigue Fract. Eng. Mater. Struct. 10 (1987) 363–372, doi:10.1111/j.1460-2695.1987.tb00486.x.

[36] Z. Zhu, S. To, W.L. Zhu, P. Huang, X. Zhou, Int. J. Mach. Tools Manuf. 136 (2019) 62–75, doi:10.1016/j.ijmachtools.2018.09.003.

[37] G.R. Johnson, in: Proceedings of the 7th International Symposium on Ballistics, 1983, pp. 541–547. http://ci.nii.ac.jp/naid/20000193157/en/.

[38] M. Aydın, Int. J. Mater. Form. 14 (2021) 1005–1018, doi:10.1007/s12289-021-01617-9.

[39] G.R. Johnson, W.H. Cook, Eng. Fract. Mech. 21 (1985) 31–48, doi:10.1016/0013-7944(85)90052-9.

[40] H. Xu, Y. Zhang, R. Peng, L. Zhu, Y. Lu, Eng. Fail. Anal. 129 (2021) 105735, doi:10.1016/J.ENGFAILANAL.2021.105735.

[41] X. Ruibin, H. Wu, Int. J. Adv. Manuf. Technol. 86 (2016) 1311–1317, doi:10.1007/s00170-015-8304-7.

[42] S. Arefin, X. Zhang, D.W.K. Neo, A.S. Kumar, Int. J. Mech. Sci. 208 (2021) 106673, doi:10.1016/J.IJMECSCI.2021.106673.

[43] W. Chen, L. Zheng, X. Teng, K. Yang, D. Huo, Int. J. Adv. Manuf. Technol. 105 (2019) 4539–4549, doi:10.1007/s00170-019-03402-0.

[44] H. Du, T. Yin, W.S. Yip, Z. Zhu, S. To, Mater. Lett. 299 (2021) 130041, doi:10.1016/j.matlet.2021.130041.

[45] C.Y. Peng, C.W. Hsu, C.W. Li, P.L. Wang, C.C. Jeng, C.C. Chang, G.J. Wang, ACS Appl. Mater. Interfaces 10 (2018) 9858–9864, doi:10.1021/acsami.8b00292.

[46] M. Marton, M. Vojs, E. Zdravecká, M. Himmerlich, T. Haensel, S. Krischok, M. Kotlár, P. Michniak, M. Veselý, R. Redhammer, J. Spectrosc. 1 (2013), doi:10.1155/2013/467079.

[47] Y.G. Gogotsi, A. Kailer, K.G. Nickel, Nature 401 (1999) 663–664, doi:10.1038/44323.

[48] Z. Zhang, J. Yan, T. Kuriyagawa, Int. J. Adv. Manuf. Technol. 57 (2011) 117–125, doi:10.1007/s00170-011-3289-3.